Catalysis Science & Technology

Effects of Pd ensemble size in dilute and single atom alloy PdAu catalysts for one-pot selective hydrogenation and reductive amination

Journal:	*Catalysis Science & Technology*
Manuscript ID	CY-ART-04-2025-000441.R1
Article Type:	Paper
Date Submitted by the Author:	26-May-2025
Complete List of Authors:	Lim, Kang Rui Garrick; Harvard University, Department of Chemistry and Chemical Biology; Harvard University Azizli, Toghrul; Tulane University, Department of Chemical and Biomolecular Engineering Kaiser, Selina; Harvard University, Department of Chemistry and Chemical Biology; Harvard University Aizenberg, Michael; Harvard University, Wyss Institute for Biologicsally Inspired Engineering Montemore, Matthew; Tulane University Department of Chemistry, ; Harvard University Department of Chemistry and Chemical Biology, Aizenberg, Joanna; Harvard University, Department of Chemistry and Chemical Biology; Harvard University

Effects of Pd ensemble size in dilute and single atom alloy PdAu catalysts for one-pot selective hydrogenation and reductive amination

Kang Rui Garrick Lim[1,2,*], Toghrul Azizli[3], Selina K. Kaiser[1,2], Michael Aizenberg[2], Matthew M. Montemore[3], Joanna Aizenberg[1,2,*]

[1] Department of Chemistry and Chemical Biology, Harvard University, Cambridge, Massachusetts 02138, United States

[2] John A. Paulson School of Engineering and Applied Sciences, Harvard University, Cambridge, Massachusetts 02138, United States

[3] Department of Chemical and Biomolecular Engineering, Tulane University, New Orleans, Louisiana 70118, United States

* Corresponding author. Email: Garrick_lim@g.harvard.edu (K.R.G.L.), jaiz@seas.harvard.edu (J.A.)

ABSTRACT

In the one-pot reaction between nitroarenes, aldehydes, and hydrogen, the desired outcome is the selective hydrogenation of nitroarenes to form aminoarenes that condense with aldehydes to form pharmaceutically relevant imines and *N*-alkylamines. One approach to facilitate the selective hydrogenation of nitroarenes over aldehydes involves using bimetallic catalysts with near equimolar ratios. However, structural characterization of metallic ensembles on the nanoparticle surface is challenging at such high alloying ratios, which hinders the elucidation of clear structure–property relationships. Here, we prepared a well-controlled series of dilute Pd-in-Au alloy catalysts with a fixed nanoparticle size as a model system to investigate the effects of surface Pd ensemble size, from single atoms to dimers and trimers, in the one-pot hydrogenation reaction between nitrobenzene and benzaldehyde as our probe reaction. The highest (near unity) selectivity to condensation products was achieved using the catalyst with the lowest Pd content prepared (Pd_2Au_{98}/SiO_2), which predominantly exposed surface Pd single atoms as verified by surface-sensitive spectroscopy. Theoretical calculations reveal that Pd single atoms were inactive for benzaldehyde adsorption and thus enabled selective nitrobenzene hydrogenation. On the contrary, the adsorption of benzaldehyde became stronger than nitrobenzene for Pd trimers and larger ensembles, explaining the enhanced competitive adsorption from benzaldehyde with increasing Pd content. Our results demonstrate that the commonly used (near equimolar) alloying ratio is rather arbitrary and may not necessarily produce the highest selectivity to condensation products. Instead, we illustrate how nanoscale Pd ensemble size control tunes competitive kinetics to steer selectivity towards forming the desired condensation products.

KEYWORDS: bimetallic, single atom alloys, PdAu, ensemble size, geometric effect, hydrogenation, cascade reactions

INTRODUCTION

Chemoselective hydrogenation of substituted nitroarenes (R-Ar-NO_2) to aminoarenes (R-Ar-NH_2) is an important industrial transformation[1,2] but challenging to perform when other reducible groups are present as a substituent (*e.g.,* carbonyl, alkene, or nitrile groups)[3–9] and/or as separate reactants (*e.g.,* aldehydes).[10–21] One such scenario requiring selective nitro group hydrogenation in the presence of other reducible groups or reactants is the one-pot reaction containing nitrobenzene (NB) and benzaldehyde (BA) in **Fig. 1**, whereby NB hydrogenation to aniline (AN) is followed by condensation with BA to form imines (IM) and their reduction products (*N*-alkylamines, AM) for the pharmaceutical and fine chemical industries.[10–21] Maximizing the selectivity towards IM and AM requires the suppression of undesired hydrogenation of BA to benzyl alcohol (BOH) and the hydrogenolysis of BA or BOH to toluene (TOL). When highly selective, a one-pot reaction simplifies separation and purification procedures while reducing the safety risks and financial cost associated with transportation and storage of intermediates, as compared to performing the reactions sequentially.[22] Most importantly, a one-pot reaction is the only option when the competing reducible group cannot be physically separated from the nitro group on the same reactant molecule (*e.g.,* 4-nitrobenzaldehyde).[17,20] These aforementioned reasons motivate our study to improve selective nitro group hydrogenation under one-pot conditions.

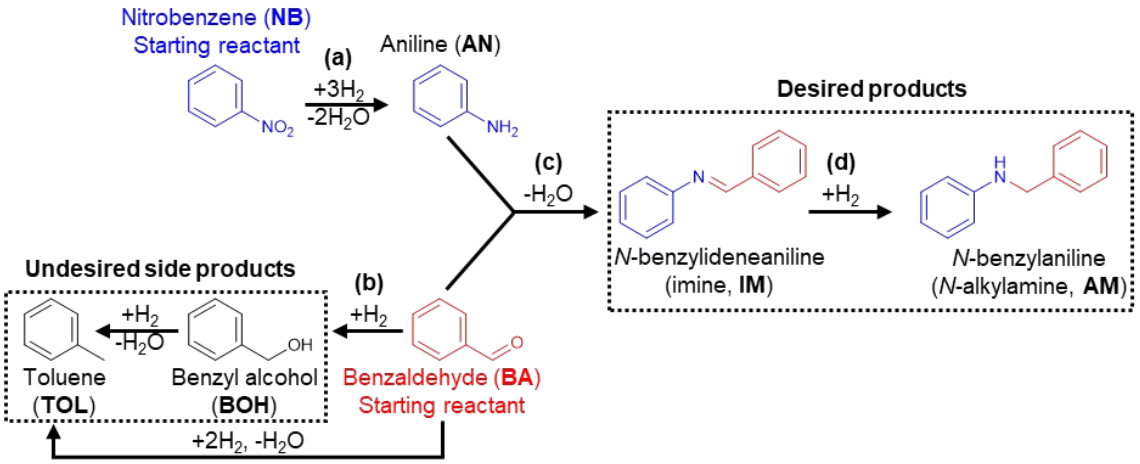

Fig. 1: Reaction scheme for one-pot selective hydrogenation and reductive amination of nitrobenzene (NB) and benzaldehyde (BA). In a successful one-pot reaction, (a) NB is competitively hydrogenated over BA to form AN, which then (c) condenses with BA to form IM. Under hydrogenation conditions, (d) IM can be further hydrogenated to AM. An undesired side reaction entails (b) BA hydrogenation to BOH, which itself may undergo hydrogenolysis to TOL. Conversion of BA to undesired products (BOH or TOL) reduces the quantity of BA available for condensation with AN, thus compromising the yield of desired products (IM and AM).

In this regard, recent advances in selective nitro group hydrogenation (over carbonyl groups) entail structural design (*e.g.,* core-shell structures, intermetallics),[12,21] support and interfacial effects,[16,18–20] and nanoparticle (NP) alloying.[9–17] Bimetallic NP alloy catalysts break up the NP surface into smaller metallic ensembles to modify their adsorption energetics to nitroarenes and aldehydes.[1] However, these studies often employ a near equimolar alloying ratio [*e.g.,* $Pt_{50}Co_{50}$ (ref. [10]), $Ni_{60}Sn_{40}$ (ref. [14]), $Pd_{50}Au_{50}$ (ref. [16])] that renders the structural characterization of surface metal ensembles too complex to study,[23] consequently precluding the derivation of clear structure–property relationships to guide catalyst designs and understand similarly complex reaction networks.

Towards this effort, we previously varied the NP composition of dilute Pd-in-Au alloy catalysts to tune the size of Pd ensembles (from single atoms to dimers and trimers) on the NP surface. Using this approach, we unambiguously investigated the effects of surface Pd ensemble size for selective alkyne hydrogenation,[24] 1-hexene isomerization,[25] H_2–D_2 exchange,[26] and BA hydrogenation.[27] In particular, we established that BA adsorption was energetically unfavorable on Pd single atoms but became increasingly facile on larger Pd ensembles due to co-adsorption of the BA aromatic ring with the carbonyl group on larger Pd ensembles.[27] Building on that specific work,[27] we hypothesize here that the Pd ensemble size can be optimized to competitively favor NB adsorption over BA in the one-pot hydrogenation–condensation reaction to selectively yield IM and AM.

In this work, we fabricated a series of Pd_xAu_{100-x}/SiO_2 (x = 0, 2, 4, 8, 12, 20, 100) catalysts and characterized the surface Pd ensemble size distribution using surface-sensitive infrared spectroscopic analysis. By testing each catalyst separately for BA hydrogenation, NB hydrogenation, and the one-pot reaction, and then comparing their kinetic data, we elucidated the role of the different surface Pd ensemble sizes on the overall selectivity of the one-pot hydrogenation–condensation reaction. Our results highlight the importance of controlling the size of Pd ensembles on the Pd_xAu_{100-x} NP surface to tune individual reaction kinetics,

maximize atomic efficiency, and direct selectivity towards the pharmaceutically relevant condensation products (IM and AM). More broadly, this work exemplifies the applicability of well-defined dilute and single atom alloy catalysts as a model system to interrogate surface ensemble size effects in catalysis.[28–31]

RESULTS AND DISCUSSION

Preparation of Pd_xAu_{100-x}/SiO_2 catalyst series. We adopted our raspberry-colloid-templating method to fabricate a series of thermally stable and mechanically robust Pd_xAu_{100-x}/SiO_2 catalysts.[32–36] The method involves attaching pre-formed colloidal Pd_xAu_{100-x} NPs to polymeric templating colloids to form composite colloids which were self-assembled and then infiltrated with a SiO_2 sol-gel precursor. The as-formed colloidal crystal was calcined to remove the templating colloids and produce a 3D macroporous catalyst with alloyed NPs partially embedded within the inner walls of the SiO_2 support for enhanced stability against sintering during catalysis.[37,38] We refer interested readers to our earlier work[37] where we extensively visualized and quantified NP embedding levels in our catalysts using electron tomography. Separately, we remark that in the preparation of Pd_xAu_{100-x} NPs, we deliberately employed a seed-mediated approach to carefully reduce a very small volume (< 2 mL) of dilute Pd^{2+} precursor (10 mM) in a large volume (240 mL) of pre-formed colloidal Au NPs that acted as nucleation sites.[39] This precautionary step was taken to avoid unwanted side nucleation of Pd NPs[34,39] while controlling the final NP size by taking advantage of the well-developed colloidal synthesis of uniformly-sized Au NPs.[40]

Across the NP composition range produced, the catalysts possessed a similar overall morphology comprising homogeneously alloyed and uniformly sized 6.5 nm PdAu NPs within a macroscopic SiO_2 support (**Fig. 2a–c, S1**).[27] The unchanged NP size across the NP composition range minimizes NP size effects on catalytic performance.[33,41,42] Notably, by linearly scaling the volume of Pd^{2+} precursor (*i.e,* Na_2PdCl_4) added during synthesis, the Pd content in the bimetallic NPs can be scaled proportionately from Pd_2Au_{98} to $Pd_{20}Au_{80}$, as verified by elemental analysis separately using inductively coupled plasma-mass spectrometry (ICP-MS, **Fig. 2d**) and X-ray photoelectron spectroscopy (XPS, **Table S1**). There was no statistical difference between the *bulk-averaged* ICP-MS and the *near NP-surface* XPS elemental composition results in **Table S1**, suggesting no appreciable Pd segregation or clustering on the NP surface. This result corroborates with the energy dispersive X-ray spectroscopy (EDX) elemental maps in **Fig. S1c** that visually depict homogeneous NP alloying in all the bimetallic NP catalysts produced. We posit that the homogeneous PdAu alloying is due to the low Pd content (2–20 molar %) of our catalysts, as Pd clustering was observed only when preparing catalysts with a higher (> 25 molar %) Pd content.[43] Separately, XPS (**Fig. 2e–f, S2**) revealed that both Pd and Au existed in their native metallic oxidation states for all bimetallic catalysts[27] while the monometallic Pd catalyst existed in an oxidized state (PdO_x),[44] consistent with our prior works.[27,44] For completeness, the fitted XPS peak dataset is provided in **Table S2**.

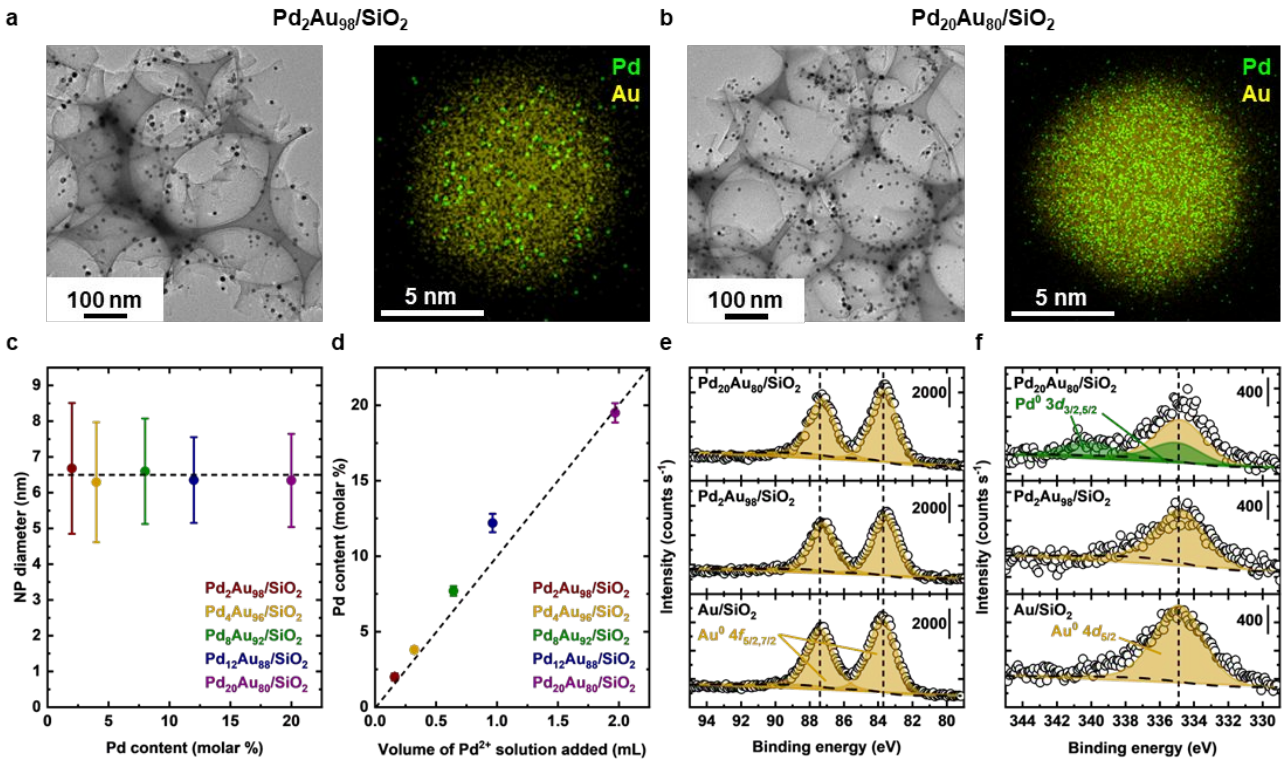

Fig. 2: Physical characterization of Pd_xAu_{100-x}/SiO_2 catalysts. (a)–(b) Transmission electron microscopy (TEM) image on the left and scanning transmission electron microscopy-energy dispersive X-ray spectroscopy (STEM-EDX) elemental maps on the right: (a) Pd_2Au_{98}/SiO_2, (b) $Pd_{20}Au_{80}/SiO_2$. (c) NP size distribution as a function of Pd content in catalysts, presented as mean ± standard deviation from 300 NPs of each catalyst using their TEM images. (d) Experimentally determined Pd content in catalysts by inductively coupled plasma-mass spectrometry (ICP-MS) elemental analysis, as a function of the volume of Pd^{2+} solution added during synthesis. Data is presented as mean ± standard deviation from three technical replicates (*i.e.,* three digested aliquots of the same catalyst). (e) Au 4*f* and (f) Pd 3*d* XPS data after peak deconvolution. The full XPS dataset is provided in **Fig. S2** and **Table S2**. For Pd_2Au_{98}/SiO_2, the Pd 3*d* XPS peaks are too low in intensity (due to the low Pd content) and hence, are not shown in (f). XPS spectra are vertically offset for clarity. Dashed lines in (c)–(f) are guides to the eye.

To characterize the surface Pd ensembles in the bimetallic catalysts, we employed diffuse reflectance infrared Fourier-transform spectroscopy (DRIFTS) using CO as a probe molecule to identify the different CO binding geometries on the NP surface.[33,45,46] Spectra taken after full CO saturation adsorption (to minimize any coverage-dependent effects[47,48]) and the subsequent Ar purging step are shown in **Fig. S3** and **Fig. 3a**, respectively. The spectra after Ar purging depict various CO coordination modes as indicated by vertical droplines in **Fig. 3a**: CO atop a single atom of Au^0 (CO-1Au^0, 2130 cm^{-1}) or Pd^0 (CO-1Pd^0, 2085 and 2070 cm^{-1}), CO bridging Pd^0 dimers (CO-2Pd^0, 1978 cm^{-1}), and CO bound to Pd^0 trimers (CO-3Pd^0, 1963 cm^{-1}).[33] The broad and asymmetric CO-1Pd^0 peak was further deconvoluted to CO bound to Pd single atoms in close proximity (2085 cm^{-1}),[49,50] and to CO bound to more dispersed Pd single atoms that experienced weaker lateral effects[51] (2070 cm^{-1}) which explains its red-shift.[52] As expected, Pd_2Au_{98}/SiO_2 exhibited a strong CO-1Au^0 peak accompanied by a weak 2070 cm^{-1} CO-1Pd^0 peak, reflective of the highly dilute Pd-in-Au NP composition. With increasing Pd content, the CO-1Au^0 peak intensity decreased considerably while CO adsorption peaks on Pd intensified.[50] Specifically, the CO-1Pd^0 peak intensity

increased before the CO-2Pd^0 and CO-3Pd^0 peaks. Also, the CO-1Pd^0 peak sharpened as its maximum shifted from 2070 cm^{-1} in Pd_2Au_{98}/SiO_2 to 2085 cm^{-1} in $Pd_{20}Au_{80}/SiO_2$, revealing that a majority of Pd atoms were in close proximity to each other on the $Pd_{20}Au_{80}$ NP surface.

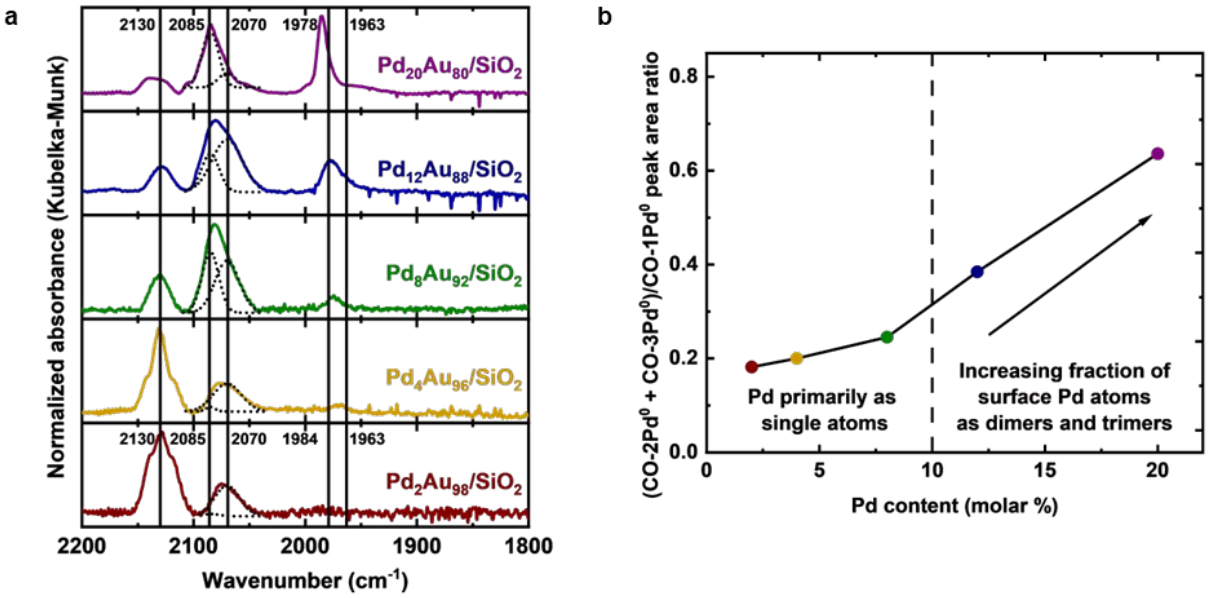

Fig. 3: DRIFTS characterization of surface Pd ensembles in Pd_xAu_{100-x}/SiO_2 catalysts. (a) DRIFTS spectra of Pd_xAu_{100-x}/SiO_2 catalysts acquired after 30 min of Ar purging following CO saturation. Spectra are vertically offset for clarity and vertical droplines indicate the different CO binding geometries on the NP surface: CO linearly bound atop a single atom of Au^0 (CO-1Au^0, 2130 cm^{-1}) or Pd^0 (CO-1Pd^0, 2085 cm^{-1} and 2070 cm^{-1}), CO bridging two adjacent Pd^0 atoms (CO-2Pd^0, 1978 cm^{-1}), and CO on a three-fold Pd^0 trimer site (CO-3Pd^0, 1963 cm^{-1}). The CO-1Pd^0 peak was deconvoluted to two features, as shown in the black dotted curves, one for Pd single atom sites in close proximity to each other (2085 cm^{-1}), and one for more dispersed Pd single atom sites that experiences weaker lateral effects (2070 cm^{-1}). (b) DRIFTS peak area ratio of Pd ensembles (*i.e.,* dimers and trimers) to Pd single atoms, as a function of Pd content in the Pd_xAu_{100-x}/SiO_2 catalysts. Dotted line indicates the estimated Pd content from which an elevated proportion of surface Pd dimers and trimers begins to show.

As we established in our earlier work[27] that BA binding was weaker on Pd single atoms but energetically more feasible on larger Pd ensembles, we quantified the peak area ratio of Pd ensembles (*i.e.,* dimers and trimers) to Pd single atoms. In **Fig. 3b**, the Pd ensemble to single atom ratio was largely unchanged from x = 2–8, before steadily increasing from $x \geq 12$. This trend in **Fig. 3b** suggests that catalysts with a low Pd content (x = 2–8) may effectively suppress BA adsorption, which would lead to selective NB hydrogenation to form the desired IM and AM in the one-pot reaction. However, we posit that the Pd content cannot be too low which would impede the NB hydrogenation rate and thus, IM and AM formation rates. Hence, we hypothesize that an optimal PdAu composition exists to maximize IM and AM yield per unit Pd mass and time. To validate our hypothesis, we tested each catalyst separately for BA and NB hydrogenation to extract their individual kinetic parameters and correlate them to their catalytic performance in the subsequent one-pot reaction.

Separate catalytic evaluation for BA and NB hydrogenation. BA[27,33,34,53] and NB[13] hydrogenation tests were separately performed to investigate the effects of NP composition on their individual conversion kinetics. Briefly, powdered catalysts and a liquid reaction feed comprising 50 mM of reactant (BA *or* NB) and 20 mM of o-xylene (internal standard) in 32

mL isopropanol solvent was loaded into a 50 mL reaction vessel. The vessel was sealed, purged with Ar gas, charged with 10 bar of H_2 gas, and then heated to 150 °C. The reaction mixture was continuously stirred at 1000 rpm to eliminate external mass transport limitations (**Fig. S4**). Sample aliquots were withdrawn at specified time intervals and analyzed by gas chromatography-mass spectrometry (sample chromatograms and mass spectra in **Fig. S5**). Details of the catalytic testing procedure are described in the **Methods** section.

The conversion-time plots and selectivity distribution at full reactant conversion are shown in **Fig. S6a–b** (for BA hydrogenation) and **Fig. S6c–d** (for NB hydrogenation). In both reactions, increasing the Pd content increased their respective first order rate constants (k_{NB} or k_{BA}, **Fig. S6e**). Au/SiO_2 was practically inactive for both NB and BA hydrogenation under our applied reaction conditions (**Fig. S6a, S6c**), confirming that Pd atoms and ensembles on the PdAu NP surface were the predominant active sites for reactant binding and reaction (which we verified computationally in **Fig. 6d** later). We remark that the poor activity of Au/SiO_2 was also recorded in other works for NB[54,55] and BA[27,34] hydrogenation, but its activity can be improved by changing the redox properties of the support[56,57] or by changing the solvent (as the dielectric constant modulates the strength of reactant adsorption).[58] Whereas AN was the sole product of NB hydrogenation (**Fig. S6d**), BA hydrogenation produced BOH and TOL in various fractions depending on the NP composition (**Fig. S6b**), consistent with our earlier work.[27]

As Au/SiO_2 was inactive for both NB and BA hydrogenation under our applied reaction conditions (**Fig. S6a, S6c**), we computed the Pd mass-normalized specific activity (SA) to compare the intrinsic catalytic activity of each hydrogenation reaction. Interestingly, SA_{NB} and SA_{BA} displayed opposite trends as a function of NP composition and, by extension, the surface Pd ensemble size (black curves in **Fig. 4a**); NB and BA hydrogenation was intrinsically more active in catalysts with lower and higher Pd contents, respectively. The SA_{BA} trend corroborates with our earlier work that Pd single atoms, primarily found in catalysts with low Pd contents, were practically inactive for BA hydrogenation under our applied reaction conditions (**Note S1**).[27] Conversely, the SA_{NB} trend indicates that atomic efficiency for NB hydrogenation was optimized with isolated Pd single atoms.

We thus predict that, in the one-pot reaction containing NB and BA, selectivity towards the desirable products (IM and AM) will be maximized using Pd_2Au_{98}/SiO_2, which recorded the highest SA_{NB}/SA_{BA} ratio (red curve in **Fig. 4a**) as an indicator for selective NB hydrogenation over BA. Note that we also calculated the SA_{NB}/SA_{BA} ratio on a per mole of metal (*i.e.,* Pd + Au) basis and verified that the trend persisted too (**Fig. S6f**). Our prediction was further substantiated by the fact that Pd_2Au_{98}/SiO_2 exhibited one of the highest NB to BA rate constant ratios (k_{NB}/k_{BA}, **Fig. 4b**) amongst the bimetallic catalysts we prepared.

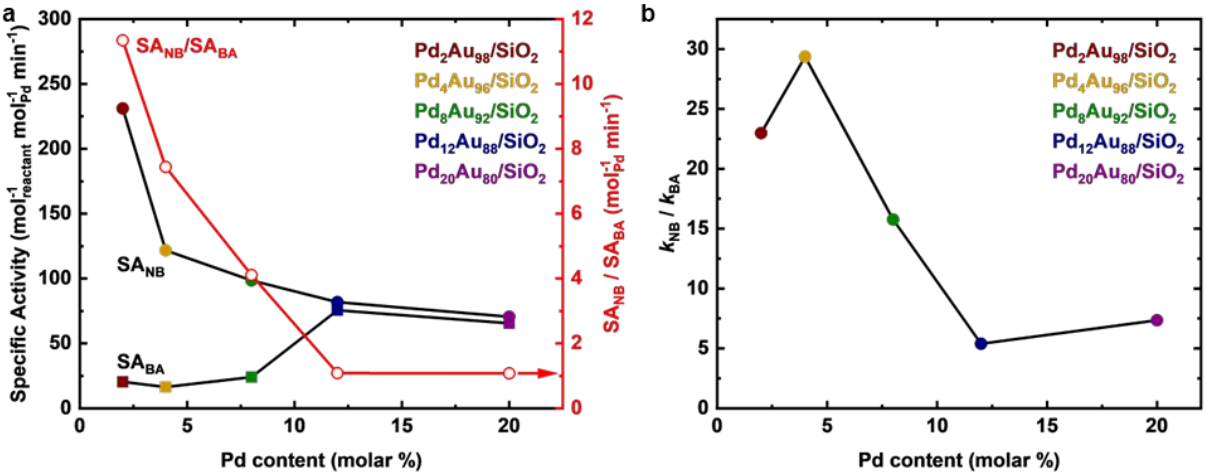

Fig. 4: Separate BA and NB hydrogenation over Pd_xAu_{100-x}/SiO_2 catalysts. (a) Pd mass-normalized specific activity of BA (SA_{BA}, filled squares) and NB (SA_{NB}, filled circles) hydrogenation reactions as a function of Pd content in Pd_xAu_{100-x}/SiO_2 catalysts. Red curve indicates the calculated SA_{NB}/SA_{BA} ratio. (b) Ratio of the NB to BA hydrogenation rate constant (k_{NB}/k_{BA}) as a function of Pd content in Pd_xAu_{100-x}/SiO_2 catalysts.

One-pot selective hydrogenation and reductive amination. We tested our prediction in a one-pot reaction.[14,15] Compared to the separate batch hydrogenation tests earlier where 50 mM of *either* BA *or* NB was used, the one-pot reaction included *both* BA (50 mM) *and* NB (50 mM) in the same solvent. There were no changes to all other reaction conditions apart from including both BA *and* NB in the same reactor. The one-pot reaction was similarly performed in 10 bar of H_2 to ensure that any hydrogenation was not limited by the quantity of dissolved H_2 in the liquid reaction feed (which we verified by varying the H_2 partial pressure[34]), although an accompanying result was that IM would be readily hydrogenated to AM too.[11,16] Nevertheless, both condensation products (IM and AM) were desirable due to their relevance to the pharmaceutical and fine chemicals industries.[14,15] No NP leaching or physicochemical differences in terms of catalyst morphology, NP size distribution, and NP composition were recorded in our post-catalytic characterization of the used catalysts (**Fig. S7, Table S3**). Hence, differences in catalytic performance were unlikely to be due to catalyst deactivation. This high thermocatalytic stability was attributed to the partial NP embedding within the SiO_2 support to resist NP sintering, migration, and leaching.[37,38,59] The concentration-time plot of all reactant species is provided in **Fig. S8**, with a good carbon balance (100 ± 10%) recorded throughout the reaction for all catalysts.

Catalytic selectivity and yield from the one-pot reaction at t = 24 h are shown in **Fig. 5**. While full NB conversion was achieved within 6 h for all the bimetallic catalysts we prepared (**Fig. S9a**), we focused our analysis on t = 24 h. This time point afforded more than sufficient time for all other reactions to proceed (*e.g.,* BA condensation with AN to form IM, IM hydrogenation to AM, BA hydrogenation to BOH and TOL) and thus, evaluate our catalysts under extended batch reaction conditions used industrially. For completeness, the concentration-time plots of all species at all time points for all catalysts are provided in **Fig. S8**, together with catalytic data analyses at full NB conversion for each catalyst in **Fig. S9**.

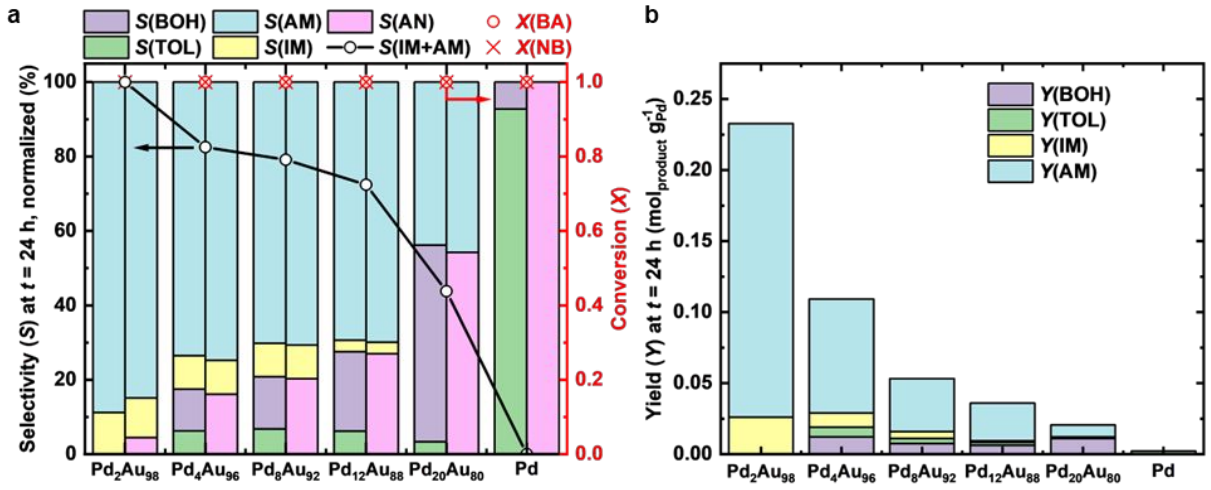

Fig. 5: One-pot selective hydrogenation and reductive amination of NB and BA over Pd_xAu_{100-x}/SiO_2 catalysts. (a) Product selectivity (*S*) distribution as a function of Pd content at t = 24 h. For each catalyst, selectivity was normalized (to a total selectivity of 100%) and separately calculated for BA-related products (BOH, TOL, IM, AM; left stacked bar) and NB-related products (NB, AN, IM, AM; right stacked bar). Open black circles represent the combined selectivity to the desirable condensation products (IM and AM). BA and NB conversion (*X*) levels are shown in open red circles and crosses, respectively. (b) Pd mass-normalized yield (*Y*) of selected products at t = 24 h, as a function of Pd content in Pd_xAu_{100-x}/SiO_2 catalysts.

In the one-pot reaction, the selectivity distribution at t = 24 h for BA-related and NB-related products were separately calculated (see left and right stacked bars for each catalyst in **Fig. 5a**). As predicted, selectivity towards the desirable IM and AM increased as the Pd content in the catalysts decreased (open black circles in **Fig. 5a**). For Pd_2Au_{98}/SiO_2, the combined selectivity to IM and AM was near-unity with no undesired BA hydrogenation products (BOH and TOL) detected, indicative of its high suitability for the one-pot reaction. Pd_4Au_{96}/SiO_2 and Pd_8Au_{92}/SiO_2 exhibited ≈80% combined selectivity to IM and AM, but BA hydrogenation products were present in appreciable quantities (≈20% combined selectivity to BOH and TOL, purple and green bars in **Fig. 5a**) which resulted in reduced BA availability and thus, more unreacted AN at the end of the reaction. For $Pd_{20}Au_{80}/SiO_2$, its combined selectivity to IM and AM was substantially lower at 43% due to pronounced undesired hydrogenation of BA (to BOH and TOL, 57% combined). Finally, monometallic Pd/SiO_2 produced no IM and AM at all, verifying the importance of bimetallic alloying to produce the desired condensation products. In line with the selectivity results, the Pd mass-normalized combined yield to IM and AM decreased with increasing Pd content in the catalysts (**Fig. 5b**), corroborating with the increased formation of unwanted BA hydrogenation products (BOH and TOL) that left an increased amount of unreacted AN. The one-pot reaction results validate our hypothesis from the separate hydrogenation tests (in the previous section) that catalysts with low Pd contents (*e.g.,* Pd_2Au_{98}/SiO_2) favored the selective hydrogenation of NB over BA to steer overall selectivity in the one-pot reaction towards IM and AM.

Pd ensemble size affects competitive reactant adsorption. We sought to rationalize the effects of surface Pd ensemble size, which was controlled by NP composition, on the one-pot reaction selectivity, by considering their relative kinetic rates. Summarily, we quantified the kinetic rates of each separate reaction step in the one-pot reaction (as depicted in **Fig. 1**): (a) NB hydrogenation, (b) BA hydrogenation, (c) condensation between BA and AN (noting

that this reaction is not Pd-catalyzed and occurs homogeneously in the solution phase), and (d) IM hydrogenation. Kinetic analysis of each individual reaction in **Fig. S10** reveals that the rates of (a) NB hydrogenation and (b) BA hydrogenation were much lower than that of (c) condensation between BA and AN and (d) IM hydrogenation, qualitatively consistent with observations from other groups.[13,15,21] This result also explains why AN dimerization does not occur,[1,9] as any formed AN would rapidly condense with BA to produce IM instead.

Following these results, we focused our analysis on the rate limiting steps of NB and BA hydrogenation, which, in turn, are governed by their competitive adsorption kinetics. We remark that IM adsorption is unlikely to play a critical role in BA or NB adsorption as the AM production rate is appreciably higher (**Fig. S10**), suggestive of a much shorter lifetime for IM adsorbed on the NP surfaces. Therefore, we intuitively posit that in the one-pot reaction, competitive adsorption between BA and NB would reduce both the rate of NB hydrogenation and availability of BA (by forming the unwanted products BOH and TOL), resulting in a lower selectivity towards IM and AM.[10,11]

Hence, we compared kinetic data in the NB-only hydrogenation reaction and the one-pot reaction to determine if the NB conversion rate and rate constant was altered by the presence of BA, as guided by related competitive adsorption kinetic studies.[60,61] In general, the presence of BA lowered the NB conversion rates, evident from comparing k_{NB} in **Fig. 6a**: k_{NB} in the one-pot reaction was up to four times smaller than k_{NB} in NB-only separate hydrogenation tests for all bimetallic catalysts except Pd_2Au_{98}/SiO_2. The difference in k_{NB} values also widened with increasing Pd content, suggesting that competitive adsorption of BA on Pd sites was most pronounced in $Pd_{20}Au_{80}/SiO_2$ (*i.e.,* the catalyst with the largest surface Pd ensemble sizes). To further verify these competitive adsorption effects, we repeated the one-pot reaction with double the initial concentration of BA (100 mM). Indeed, k_{NB} was unaffected in Pd_2Au_{98}/SiO_2 (**Fig. 6b**) but decreased even further for $Pd_{20}Au_{80}/SiO_2$ (**Fig. 6c**). These results not only validate the competitive adsorption effects of BA present in $Pd_{20}Au_{80}/SiO_2$, but also illustrate that, on catalysts with high Pd contents, a higher initial BA concentration reduces NB conversion rates even further by exacerbating these effects.

To understand why competitive adsorption was negligible for catalysts with low Pd contents (*e.g.,* in Pd_2Au_{98}/SiO_2) but more pronounced in catalysts with higher Pd contents (*e.g.,* in $Pd_{20}Au_{80}/SiO_2$), we performed separate theoretical calculations of NB and BA adsorption over different Pd ensemble sizes. Here, we remark that calculating the full reaction pathway would be computationally challenging and expensive, and we reason that on weakly binding surfaces such as dilute Pd-in-Au alloys, the reaction rate ratio is most likely controlled by reactant adsorption.[27] Guided by DRIFTS results in **Fig. 3** that indicated surface Pd ensemble sizes of 1–3 in our bimetallic catalysts, we calculated the BA and NB adsorption energies (E_{ads}), *via* aromatic ring adsorption geometries, on Au(111), Pd single atoms, dimers, and trimers in Au(111), and on Pd(111), as shown from the left to right insets in **Fig. 6d**. These surfaces represent a Pd ensemble size of zero, one, two, three, and an extended Pd surface, respectively. The main results are summarized in **Fig. 6d** with the full dataset provided in **Fig. S11**. Our calculations reveal that for both reactants, reactant binding strengthens with larger Pd ensemble sizes, indicating a stronger binding affinity of both

reactants to Pd than to Au (**Fig. 6d**).[16,27] As both reactants bind much more weakly to Au, relative to Pd, we posit that both reactants are unlikely to adsorb on Au with sufficiently long enough lifetimes to accept spillover H adatoms (from adjacent Pd ensembles on the same NP that activate H_2) to induce hydrogenation on Au surfaces of the bimetallic PdAu NPs.

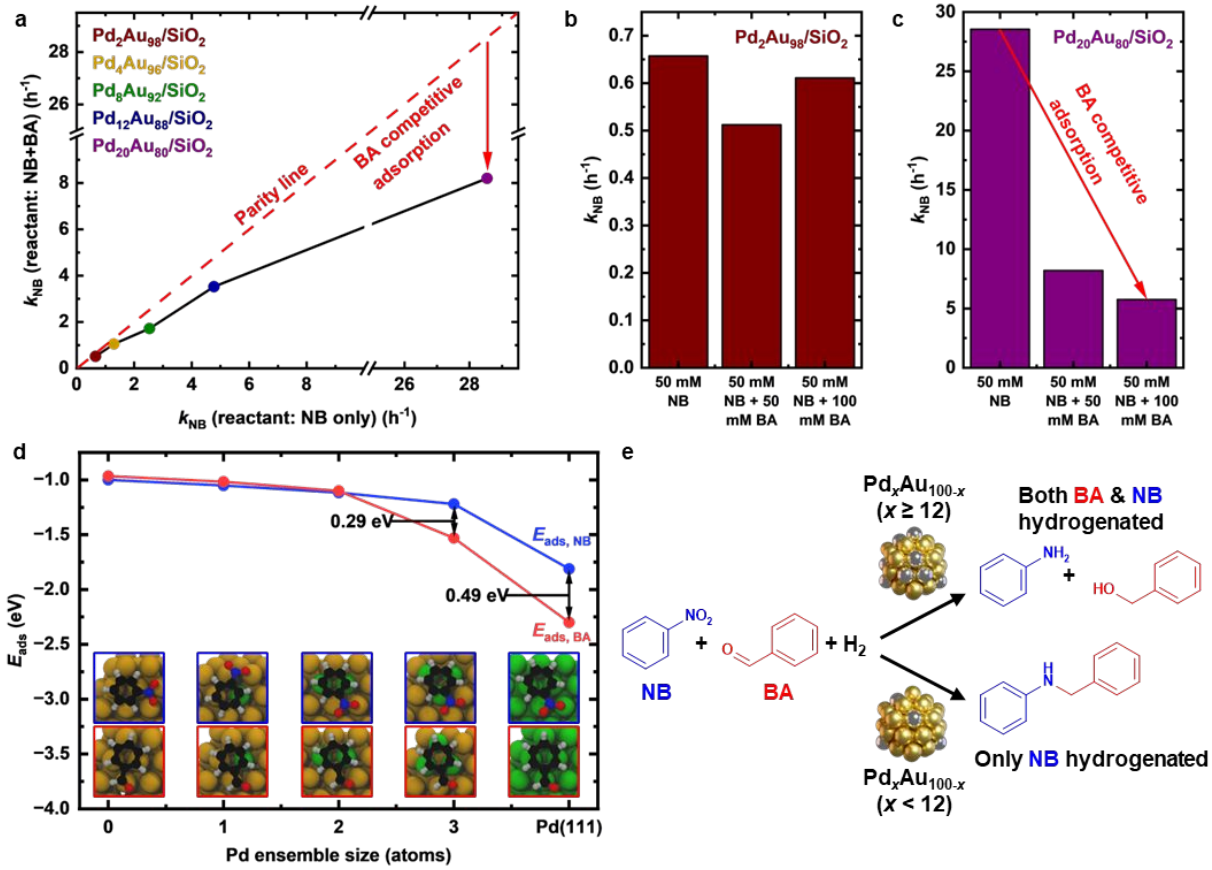

Fig. 6: Pd ensemble size affects competitive adsorption kinetics between NB and BA. (a) Plot of k_{NB} in the one-pot reaction (vertical axis) against k_{NB} in NB-only hydrogenation reaction (horizontal axis). Red dashed line is a parity line. Data points that fall below this line indicate catalysts with a smaller k_{NB} in the one-pot reaction than in the NB-only hydrogenation reaction and thus, indicative of BA competitive adsorption in the one-pot reaction. (b)–(c) k_{NB} under NB-only hydrogenation conditions (50 mM NB), one-pot conditions (50 mM NB + 50 mM BA), and one-pot conditions with double the starting BA concentration (50 mM + 100 mM BA) for (b) Pd_2Au_{98}/SiO_2 and (c) $Pd_{20}Au_{80}/SiO_2$. (d) Calculated E_{ads} values of BA and NB for Au(111), Pd_1/Au(111), Pd_2/Au(111), Pd_3/Au(111), Pd(111). Pd(111) represents monometallic Pd, which exhibits extended Pd ensembles. Insets below the data points depict the respective binding geometries for NB (blue boxes) and BA (red boxes), with gold, green, black, grey, blue, red spheres representing Au, Pd, C, H, N, and O, atoms, respectively. (e) Effect of Pd_xAu_{100-x} NP composition and, by extension, the surface Pd ensemble size, on competitive adsorption kinetics between NB and BA in the one-pot reaction.

In **Fig. 6d**, E_{ads} of BA and NB were comparable on Pd single atoms and dimers, agreeing with the largely unchanged k_{NB} and thus, negligible competitive adsorption effects for Pd_2Au_{98}/SiO_2, Pd_4Au_{96}/SiO_2, and Pd_8Au_{92}/SiO_2 as seen in **Fig. 6a**. However, on Pd trimers and extended Pd surfaces, E_{ads} of BA was substantially more energetically favorable than NB (by ≈0.3–0.5 eV, **Fig. 6d**), which was a trend that we reproduced using other relevant adsorption geometries of NB and BA too (**Fig. S12–S13**). These calculation results suggest a higher probability for BA to outcompete NB for adsorption on Pd trimers and larger

ensemble sites. Our results are also consistent with the reduced k_{NB} in the one-pot reaction compared to NB-only hydrogenation for catalysts with higher Pd contents such as $Pd_{12}Au_{88}/SiO_2$ and $Pd_{20}Au_{80}/SiO_2$ (**Fig. 6a**), together with the increased BA competitive adsorption effects on $Pd_{20}Au_{80}/SiO_2$ when the starting BA concentration was doubled (**Fig. 6c**). Since $Pd_{12}Au_{88}/SiO_2$ and $Pd_{20}Au_{80}/SiO_2$ exhibit a three-fold increase in their Pd ensemble to single atom ratio (compared to Pd_2Au_{98}/SiO_2, Pd_4Au_{96}/SiO_2, and Pd_8Au_{92}/SiO_2) in **Fig. 3b**, we attribute the increased BA hydrogenation rates and competitive adsorption effects in these catalysts primarily to these Pd trimers and larger ensembles (**Fig. S14**). Altogether, our catalytic analyses and theoretical calculations corroborate that the surface Pd ensemble size is an important descriptor for reactant adsorption and conversion kinetics.

Our findings are summarized in **Fig. 6e**. Across a series of Pd_xAu_{100-x}/SiO_2 catalysts, an increase in Pd content (x) was accompanied by higher conversion rates of both BA and NB to their hydrogenated products (**Fig. S6a, S6c**). However, not all Pd ensemble sizes were amenable to reactant binding as BA adsorption on Pd (or Au) single atoms was not facile under our applied reaction conditions,[27] resulting in low BA conversion rates for catalysts with low Pd contents ($x \leq 8$, **Fig. 4a**). The implications of these results were directly observed in the one-pot reaction of BA and NB. Catalysts with low Pd contents of $x \leq 8$, possessing predominantly Pd single atoms on their NP surfaces (**Fig. 3b**), selectively hydrogenated NB but not BA, resulting in high selectivity to the desirable IM and AM (**Fig. 5a**). Conversely, catalysts with higher Pd contents of $x \geq 12$ possessed an elevated Pd ensemble to single atom ratio on their NP surfaces (**Fig. 3b**), leading to substantial competitive BA adsorption and thus, undesired hydrogenation of BA (**Fig. S14**). This competitive adsorption effect reduced NB conversion rates (**Fig. 6a, 6c**) and BA availability, resulting in a lower selectivity to IM and AM (**Fig. 5a**). The underlying reason for the appreciable BA competitive adsorption effects in catalysts with Pd contents of $x \geq 12$ and not for $x \leq 8$ was clarified by theoretical calculations, which revealed that BA adsorption was markedly stronger than NB for Pd trimers and larger ensembles, but not for Pd single atoms (**Fig. 6d**).

CONCLUSIONS

We investigated the effects of Pd ensemble size in the one-pot selective hydrogenation and reductive amination reaction between NB and BA using a well-controlled dilute alloy Pd_xAu_{100-x}/SiO_2 (x = 0, 2, 4, 8, 12, 20, 100) catalyst series with a fixed NP size. Surface-sensitive DRIFTS analysis revealed that the ratio of surface Pd ensembles to single atoms was low and largely invariant at low Pd contents (x = 2–8) but increased three-folds from $x \geq 12$, indicating the formation of more Pd dimers and trimers on the NP surface. Next, we evaluated the NB and BA hydrogenation reactions separately to independently analyze and optimize the Pd ensemble size for a high specific activity ratio of NB to BA. The highest specific activity ratio of NB to BA was recorded for Pd_2Au_{98}/SiO_2, which we hypothesized to be a good predictor of selective NB hydrogenation over BA in the one-pot reaction. We verified this hypothesis in the one-pot reaction and found that a higher selectivity to the desirable condensation products (IM and AM) was correlated to lower Pd contents in the catalysts, consistent with the earlier separate (NB or BA) hydrogenation test results.

Crucially, near-unity selectivity to IM and AM was achieved using the catalyst with the lowest Pd content (Pd_2Au_{98}/SiO_2), validating its high suitability for the one-pot reaction.

To elucidate the effects of Pd ensemble size on catalytic selectivity in the one-pot reaction, we compared the kinetic data of each bimetallic PdAu catalyst for BA hydrogenation, NB hydrogenation, and the one-pot reaction. Compared to the NB-only hydrogenation reaction, the NB hydrogenation rate constant in the one-pot reaction was reduced with increasing Pd content in the catalysts by up to four-folds, indicative of competitive adsorption effects from BA. These competitive adsorption effects were stronger at higher Pd contents ($x \geq 12$), which also corresponded to an enrichment of non-single atom Pd ensembles (*i.e.,* dimers and trimers) on the NP surface from DRIFTS analysis. Theoretical calculations of BA and NB adsorption energetics on different Pd ensemble sizes reveal comparable binding energies of both NB and BA on Pd single atoms and dimers, whereas Pd trimers and extended ensembles energetically favor BA absorption over NB.

Together, the DRIFTS, catalytic, and theoretical analyses indicate that Pd_2Au_{98}/SiO_2 exposed predominantly Pd single atoms on their NP surfaces which were not energetically facile for BA adsorption. Consequently, this resulted in unreacted BA and unimpeded NB adsorption onto Pd single atom sites for selective NB hydrogenation, leading to high selectivity to the condensation products. Conversely, catalysts with higher Pd contents ($Pd_{20}Au_{80}/SiO_2$) exhibited substantially lower selectivity to the condensation products due to the elevated presence of large Pd ensembles on their NP surfaces that enabled (undesired) competitive adsorption of BA alongside NB to form unwanted BA hydrogenation products.

Our results illustrate that a near equimolar alloying ratio generally described in the literature[10,14,16] may not necessarily produce the highest catalytic selectivity towards the desirable condensation products (IM and AM). Here, we maximized selectivity to the condensation products using catalysts with the lowest Pd content (Pd_2Au_{98}/SiO_2), which improves both atomic efficiency and cost effectiveness. Given the strong correlation between Pd ensemble size and the strength of competitive adsorption effects observed in our one-pot reaction, we point out that the size of reactive surface ensembles on the NP surfaces of bimetallic catalysts is likely an important descriptor to predict catalytic performance in other similarly competitive reaction networks beyond this work. For instance, an earlier work investigated how the Pd ensemble size in Au/Pd(111) surface planar alloys, tuned by the amount of Au used during thermal annealing, directs the selective oxidation of crotyl alcohol to crotonaldehyde while minimizing competitive decomposition pathways.[62]

Beyond altering the PdAu NP composition as shown in this work, we highlight the complementary use of high temperature oxidative or reductive gaseous pre-treatments for adsorbate-induced Pd segregation towards or into the PdAu NP bulk, respectively, as another method to control the ratio of Pd ensembles to single atoms.[23,38,63,64] Additionally, we are investigating how nanoscale wetting phenomena at the Au/support interface plays a role in directing Pd deposition and hence, the spatial position and size distribution of Pd ensembles on the PdAu NP surface at a fixed NP composition.[65] Lastly, we remark that tracking the evolution of Pd ensembles in PdAu alloyed NPs during reaction have been realized by *in situ* imaging and spectroscopy. Pd ensemble dynamics have also been modelled at the entire NP

level using machine-learned interatomic potentials,[66–68] representing a clear and exciting advance from modelling surface planar models.

Overall, this work highlights the importance of surface metal ensemble size control to tune kinetic parameters to maximize atomic efficiency and direct catalytic outcomes.[64,69–72] With a growing number of catalytic applications involving bimetallic, multi-metallic, and even high entropy alloy catalysts,[44,73–78] we anticipate that our results will present dilute and single atom alloy catalysts as well-defined model systems with precisely tunable minority metal ensemble sizes for rational catalyst design and systematic investigations, such as to interrogate surface ensemble size effects in catalysis as demonstrated in this work (for the one-pot reaction between NB and BA) and for other relevant catalytic reaction networks.[28–31]

METHODS

Chemicals. All chemicals were used as received unless otherwise specified. Tetrachloroauric (III) acid trihydrate ($HAuCl_4 \cdot 3H_2O$, ≥99.9%), palladium (II) nitrate hydrate ($Pd(NO_3)_2 \cdot 2H_2O$, Sigma-Aldrich product code: 205761), sodium tetrachloropalladate (II) (Na_2PdCl_4, 98%), sodium citrate tribasic dihydrate (≥99.0%), sodium borohydride ($NaBH_4$, 96.0%), polyvinylpyrrolidone (PVP, 55 000 g mol^{-1}), L-ascorbic acid (≥98%), tetraethyl orthosilicate (TEOS, 98%), benzaldehyde (BA, ≥99.5%, purified by redistillation by Sigma-Aldrich, stored in Sure/Seal Sigma-Aldrich bottle in an inert environment), nitrobenzene (NB, ≥99%,), o-xylene (≥99%), isopropanol (HPLC grade, ≥99.9%), hydrochloric acid (HCl, 37%), nitric acid (HNO_3, 70%), were purchased from Sigma-Aldrich. Absolute ethanol (EtOH) was purchased from KOPTEC. Ultrapure deionized water (Millipore Milli-Q, 18.2 MΩ cm^{-1}) was used in all the experiments. All chemicals were stored under ambient conditions except $HAuCl_4$, $Pd(NO_3)_2$, Na_2PdCl_4, and $NaBH_4$, which were stored in a vacuum desiccator at room temperature. All glassware for NP synthesis was cleaned with fresh aqua regia (HCl : HNO_3 in 3:1 volume ratio) overnight, rinsed with excess water, dried at 120 °C, and left to cool to room temperature before use. **CAUTION:** HCl, HNO_3, and aqua regia are highly corrosive and should only be handled by trained users under adequate engineering controls and personal protective equipment.

Catalyst synthesis. *PVP-capped NPs (Au, Pd, or PdAu).* Monometallic Au and Pd NPs were synthesized by adapting a previously published protocol[49] with minor modifications to produce 6.5 nm (in diameter) Au and Pd NPs to avoid NP-size related effects during catalytic evaluation. To prepare Au NPs,[40] 240 mL deionized water was stirred with 1.2 mL $HAuCl_4$ solution (63.4 mM) and 0.6 mL sodium citrate solution (0.17 M) at room temperature in air in a 500 mL aqua regia-cleaned one-neck glass round bottom flask with a magnetic stir bar to produce a faint yellow solution. After 5 min of stirring, 0.72 mL $NaBH_4$ solution (containing 10 mg $NaBH_4$ in 1 mL ice cold deionized water, then add 5 mL of 0.17 M sodium citrate solution) was quickly injected to the round bottom flask and stirred overnight in the dark in air at room temperature to yield citrate-capped Au NPs. The next day, 7.2 mL PVP solution (1 g PVP in 10 mL deionized water) was added to the Au NP solution and stirred for 30 min in air before use to exchange the citrate ligands for PVP ligands.[59]

To prepare Pd NPs, we modified our previously published protocol.[49] Briefly, 8.6 g PVP was added to 150 mL deionized water in a 500 mL aqua regia-cleaned three-neck glass round bottom flask with a magnetic stir bar and stirred in air until a clear colourless solution formed. Next, 27.8 mg $Pd(NO_3)_2$ was added to the flask. All three necks of the flask were stoppered with rubber septa, stirred for 15 min and then sonicated for 15 min until all the $Pd(NO_3)_2$ solids have dissolved to form a cloudy orange-brown solution. The flask was clamped in an ice bath on top of a magnetic stirring plate. A N_2 purge needle was injected through one septum to continuously bubble N_2 into the solution while another bleed needle was injected through another septum to relief pressure build-up in the flask. After 30 min of bubbling N_2 into the solution, both needles were removed and 3 mL $NaBH_4$ solution (0.5 M) was quickly injected into the flask. At 10 min post-injection, the flask removed from the ice bath. The stoppered flask was left to stand undisturbed (without stirring) in the dark at room temperature for 48 h to yield PVP-capped Pd NPs.

PVP-capped bimetallic Pd_xAu_{100-x} NPs (x = 2, 4, 8, 12, 20; x refers to the Pd molar composition of the NPs) were prepared directly using PVP-capped Au NPs produced earlier. The flask containing 240 mL of PVP-capped Au NPs was acidified to pH 4–5 with 2.4 mL HCl solution (0.1 M) and stirred in air for 30 min. Next, 160.8/321.6/643.2/964.8/1608 μL Na_2PdCl_4 solution (10 mM) was added to the flask and stirred for 5 min, before adding 160.8/321.6/643.2/964.8/1608 μL L-ascorbic acid solution (40 mM) for x = 2/4/8/12/20. These volumes were scaled from the 160.8 μL of Na_2PdCl_4 solution and 160.8 μL of L-ascorbic acid required to Pd_2Au_{98} NPs. For instance, a 10-fold larger volume of Na_2PdCl_4 solution and its corresponding reducing agent L-ascorbic acid would be required (*i.e.,* 1608 μL) to increase the Pd content by 10-folds to produce $Pd_{20}Au_{80}$ NPs.

The flask was stirred overnight in air in the dark. UV-vis analysis of the undiluted NP solution after overnight stirring yields absorbance peaks at 517.5, 516.5, 514.5, 513.5, 510.0 nm for PVP-capped Pd_2Au_{98}, Pd_4Au_{96}, Pd_8Au_{92}, $Pd_{12}Au_{88}$, and $Pd_{20}Au_{80}$ NPs, respectively. With increasing Pd content, the absorbance peak intensity also correspondingly decreases.

Raspberry-colloid-templated catalysts. Catalysts were fabricated using our previously reported method with minor modifications.[32,79] First, an aqueous colloidal suspension of positively-charged (+35 mV) amidine-functionalized polystyrene (PS) spheres of approximately 280 ± 10 nm in diameter were prepared using a previously published method.[80] Second, PVP-capped NPs were attached to PS colloids: to 24 mL of PS colloids (5 wt % in water) in a 500 mL round bottom flask, 240 mL (for Au or Pd_xAu_{100-x}) or 60 mL (for Pd) PVP-capped NP solution was added dropwise over 1 h while stirring in air at room temperature at 400 rpm. The solution was then acidified to approximately pH 4–5 with 0.7% w/w HNO_3 and stirred for 15 min. The NP-decorated PS colloids (referred to as raspberry colloids) were centrifuged for 30 min twice at 12000 g, supernatant discarded, and the residue dispersed in 24 mL deionized water. The as-dispersed raspberry colloids were dispensed in 4 mL aliquots into separate conical vials and left undisturbed to dry at 65 °C overnight in a convection oven on a vibration-isolation table, which produced dried (raspberry) colloidal crystals. Each vial of colloidal crystal was infiltrated with 200 μL of pre-hydrolyzed TEOS mixture (TEOS : EtOH : 0.1 M HCl = 1:1:1 by volume, stirred for 1 h before use) and then

dried at 65 °C for 1 h in a convection oven, before repeating the infiltration-drying step twice more. The thrice-infiltrated and dried raspberry colloidal crystals were transferred into a glass vial and calcined in static air at 500 °C for 2 h (ramped at 10 °C min^{-1}) to yield Pd_xAu_{100-x}/SiO_2 catalysts that were crushed and sieved (106–300 μm) before use. The Brunauer-Emmett-Teller (BET) surface area by N_2 physisorption at 77 K for all catalysts was largely consistent at 250 ± 20 m^2 g^{-1} (standard deviation determined from three repeat measurements for each catalyst) and in line with our earlier works,[44,49] due to the fixed size of polystyrene templating colloids used in the synthesis of all catalysts in this work.

Physical characterization. Electron microscopy (SEM, TEM, STEM-EDX), elemental analysis (XPS, inductively coupled plasma-mass spectrometry, ICP-MS), surface-sensitive analysis (DRIFTS), and porosimetry are described in the **Supporting Methods**.

Catalytic evaluation. *Liquid phase benzaldehyde or nitrobenzene hydrogenation.* BA or NB hydrogenation tests were conducted in the same 50 mL stainless steel batch reactor (Parr 5512) following our previously published work with minor modifications.[33,34] The liquid reaction feed comprises of BA (162.6 μL) or NB (164.7 μL) and o-xylene (internal standard, 77.3 μL) in isopropanol solvent to make up a total volume of 32 mL. Using these volumes produces a liquid reaction feed of 50 mM reactant (BA or NB) and 20 mM o-xylene internal standard in isopropanol solvent. An initial aliquot of 0.15 mL was withdrawn from the liquid reaction feed for purity analysis, resulting in a final total volume of 30.5 mL.

To this liquid reaction feed, sieved catalysts (corresponding to 0.6 mg metal mass and a reactant : metal site molar ratio of ≈4300) was added. Note that the catalyst loading was fixed at 0.6 mg metal mass such that overall reaction kinetics is not too slow for low Pd content catalysts (*e.g.,* Pd_2Au_{98}/SiO_2) but also not too fast for high Pd content catalysts (*e.g.,* $Pd_{20}Au_{80}/SiO_2$). The reactor was assembled and vigorously stirred with an overhead mechanical stirrer at 1000 rpm to eliminate external mass transport limitations (which we verified by changing the stirring speed in **Fig. S4**). Internal (pore) diffusion limitations were also absent as the pore size used in this work was large (≈300 nm) and that we previously did not observe a change in the experimentally observed rates when using similar catalysts with a smaller (200 nm) or larger (500 nm) pore size.[34] Next, the reactor was purged four times with N_2 gas (99.998%, approximately 30 bar) and then pressurized three times with 10 bar of H_2 gas (99.999%) to saturate the reaction feed with H_2 and heated to 150 °C (which took ≈10 min). Note that the reaction time was set to $t = 0$ at the onset of heating to collect any reaction data that occurred during the initial ≈10 min heating ramp. The reactor was stirred for 24 h and sample aliquots of approximately 0.2 mL each were withdrawn at specified timepoints from the reactor's sampling valve and analyzed by offline gas chromatography-mass spectrometry (GC-MS) comprising of an Agilent 7890A GC (HP-1MS column, Agilent part number 19091S-933, maintained at 50°C and with flowing He at 1.4 mL/min) and an Agilent 5975C MS (operating vacuum of ≈6×10^{-6} Torr). Typically, a 10 μL aliquot was injected into the GC using an Agilent 7693 Autosampler. Then, the species in the aliquot were separated using the following 15 min GC program: hold the oven temperature at 50 °C for 3 min, then ramp to 250 °C at 20°C/min over the next 10 min, then hold at 250 °C for another 2 min.

Note that the MS detector was not switched on for the first 2 min of the GC program to avoid saturating the MS detector from the eluting isopropanol solvent.

Species were quantified using two internal calibration curves prepared in isopropanol (solvent) with o-xylene (internal standard) as shown in **Fig. S5**. The first calibration curve comprised of BA, BOH, and TOL, while the second calibration curve comprised of NB, AN, IM, and AM. After each sample withdrawal, the reactor was repressurized back to 10 bar H_2. Calculation methods for catalytic descriptors for the BA or NB hydrogenation batch reaction are shown below in equations (1)–(3).

The conversion of reactant *i* (X_i, *i* = BA or NB) at time *t* is defined by (1). Note that $[i]_{t=0}$ and $[i]_t$ refer to the concentration of reactant *i* at time *t* = 0 and time *t*, respectively.

$$X_i(\%) = \frac{[i]_{t=0} - [i]_t}{[i]_{t=0}} \times 100\% \quad eq.\,(1)$$

For BA hydrogenation, the reaction selectivity towards a specific product *i* (S_i, where *i* = benzyl alcohol, BOH or toluene, TOL) at a specific benzaldehyde conversion X_{BA} is the concentration of that specific product formed as a fraction of the concentration of benzaldehyde converted away at that time *t*, as shown in (2). Note that for nitrobenzene hydrogenation, NB is hydrogenated to aniline (AN) with 100% conversion and thus, S_{AN} = 100% for NB hydrogenation reactions.

$$S_i\,(\%) = \frac{[i]_t}{[BA]_{t=0} - [BA]_t} \times 100\% \quad eq.\,(2)$$

Pd mass-normalized specific activity (SA) was determined at *t* = 0.5 h and defined in this work by the number of moles of reactant *i* (*i* = NB or BA) consumed, the number of moles of Pd in the catalyst (by ICP-MS elemental analysis), and the reaction time, in (3) below. The mass of Pd used is calculated from the catalyst mass, metal loading in the catalyst, and NP composition. Note that 0.0305 L refers to the volume of the reactant solution in the batch reactor.

$$SA\left(mol_i\, mol_{Pd}^{-1}\, min^{-1}\right) = \frac{\#\, moles\ of\ i\ consumed}{(\#\, moles\ of\ Pd\ atoms)(30\ min)}$$
$$= \frac{([i]_{t=0} - [i]_t)(0.0305\ L)}{\left(\frac{Mass\ of\ Pd\ in\ mg \div 1000}{106.42\ g\ mol^{-1}}\right)(30\ min)} \quad eq.\,(3)$$

In the individual (BA or NB) hydrogenation tests, we confirmed in earlier works[33,34] that BA hydrogenation under the applied reaction conditions is 1st order with respect to BA concentration, [BA] due to the large excess of H_2 partial pressure applied. Thus, the 1st order rate constant for the BA hydrogenation reaction (k_{BA}) in **Fig. 4b** is calculated from the gradient of the linear plot of ln[BA] as a function of time. Following similar reasoning, we also confirmed that NB hydrogenation under the applied reaction conditions is 1st order with respect to NB concentration, [NB], consistent with other works.[6,9,15] Thus, the 1st order rate constant for the NB hydrogenation reaction [k_{NB} (reactant: NB only)] in **Fig. 4b** is calculated

from the gradient of the linear plot of ln[NB] as a function of time. To ensure that the rate constants were indicative of the initial rates, only catalytic data in the first 30 min of reaction were used for fitting the linear plot.

Liquid phase one-pot selective hydrogenation and reductive amination of benzaldehyde and nitrobenzene. The one-pot catalytic tests follow all conditions for BA or NB hydrogenation tests described earlier, with the only exception being the composition of the liquid feed. In the one-pot catalytic tests, the liquid reaction feed comprises of BA (162.6 μL), NB (164.7 μL), and o-xylene (internal standard, 77.3 μL) in isopropanol solvent to make up a total volume of 32 mL. Using these volumes produces a liquid reaction feed of 50 mM BA, 50 mM NB, and 20 mM o-xylene internal standard in isopropanol solvent. All reaction conditions (10 bar H_2, 150 °C, 24 h, stirring at 1000 rpm) remain unchanged.

In the one-pot reaction, the conversion of reactant *i* (X_i, *i* = BA or NB) at time *t* is described by (1) earlier. The reaction selectivity towards a specific product *i* (S_i, where *i* = BOH, TOL, AN, imine, IM, *N*-alkylamine, AM) was computed for each of the specific reactant BA or NB at a specific conversion X_i (*i* = BA or NB). Since BA can only form BOH, TOL, IM, and AM, the reaction selectivity towards a specific BA-related product *i* (S_i, where *i* = BOH, TOL, IM, and AM) at a specific benzaldehyde conversion X_{BA} is the concentration of that specific product (BOH, TOL, IM, and AM) formed as a fraction of the concentration of benzaldehyde converted away at that time t, as shown in (2). Conversely, since NB can only form AN, IM, and AM, the reaction selectivity towards a specific NB-related product *i* (S_i, where *i* = AN, IM, and AM) at a specific nitrobenzene conversion X_{NB} is the concentration of that specific product (AN, IM, and AM) formed as a fraction of the concentration of nitrobenzene converted away at that time *t*, as shown in (2). In this work, we calculate the BA-related product selectivity distribution and NB-related product selectivity distribution separately as X_{BA} and X_{NB} can be different at that same point in time.

The Pd mass-normalized yield of any product *i*, Y_i, is calculated by the number of moles of product *i* (*i* = BOH, TOL, IM, or AM) formed per unit mass of Pd. Product yield was calculated at a *t* = 24 h and at full NB conversion (X_{NB} = 1), as shown in (4).

$$Y_i\ \left(mol_i\ g_{Pd}^{-1}\right) = \frac{\#\ moles\ of\ i\ produced}{(mass\ of\ Pd)} = \frac{\left([i]_{t=24\ h\ or\ X(NB)=1}\right)(0.0305\ L)}{Mass\ of\ Pd\ in\ g} \quad eq.\ (4)$$

In the one-pot reaction, given that NB can only be hydrogenated to AN with no other side products, the 1st order rate constant for the NB conversion in the one-pot reaction [k_{NB} (reactant: NB+BA)], as reported in **Fig. 6a–c**, is calculated from the gradient of the linear plot of ln[NB] as a function of time. To ensure that the rate constants were indicative of the initial rates, only catalytic data in the first 30 min of reaction were used for fitting the linear plot. Computation of the rate constants for other reactants and products in the one-pot reaction is complicated by the presence of multiple products and are calculated separately in **Fig. S10**.

Theoretical calculations. Density functional theory (DFT) calculation details are described in the **Supporting Methods**.

ASSOCIATED CONTENT

Supporting Information. The Supporting Information is available free of charge online. Supporting methods, notes, experimental, and theoretical calculation results.

DATA AVAILABILITY

Data from this study are available from the authors upon reasonable request.

AUTHOR CONTRIBUTIONS

K.R.G.L. conceived the research idea and designed the experiments. K.R.G.L. synthesized, characterized, and analyzed the materials. K.R.G.L., with input from S.K.K., designed and performed the catalytic tests and analyzed the catalytic data. T.A., supervised by M.M.M., performed the theoretical calculations and analyzed the results. K.R.G.L. coordinated the entire work and wrote the manuscript with input from all authors. M.A. and J.A. supervised the entire work. All authors approve the final version of the manuscript.

COMPETING INTERESTS

The authors declare no competing financial interests.

ACKNOWLEDGEMENTS

This work was supported by the U.S. Defense Threat Reduction Agency (DTRA) under Award Number HDTRA12110016 (K.R.G.L., M.A., J.A.) and by the U.S. Department of Energy, Office of Science, Basic Energy Sciences under Award Number DE-SC0012573 (S.K.K.). T.A. and M.M.M. are supported by the U.S. National Science Foundation under Grant Number CBET-2340356. Electron microscopy and XPS analyses were performed at the Center for Nanoscale Systems (CNS), a member of the National Nanotechnology Coordinated Infrastructure Network (NNCI), which is supported by the National Science Foundation under NSF ECCS award 1541959. DRIFTS analyses were conducted in the Reactor Engineering and Catalyst Testing (REACT) Facility of the Northwestern University Center for Catalysis and Surface Science (CCSS), which is supported by the U.S. DOE under award DE-SC0001329. T.A. and M.M.M. acknowledge support from Technology Services at Tulane University, New Orleans, LA for high performance computing (HPC) resources and services. K.R.G.L. acknowledges financial support from the Agency for Science, Technology and Research (A*STAR) Singapore National Science Scholarship (PhD). S.K.K. acknowledges the Swiss National Science Foundation for the award of an Early Postdoc.Mobility fellowship (SNSF grant number: P2EZP2_199972).

REFERENCES

(1) Yao, C.; Li, W.; Ge, X.; Shi, Y.; Cao, Y.; Chen, D.; Zhou, X.; Duan, X. Mechanism and Kinetics Guided Design of Catalysts for Functionalized Nitroarenes Hydrogenation. *ChemCatChem* 2024, *16* (16), e202400027.

(2) Blaser, H.; Steiner, H.; Studer, M. Selective Catalytic Hydrogenation of Functionalized Nitroarenes: An Update. *ChemCatChem* **2009**, *1* (2), 210–221.
(3) Serna, P.; Corma, A. Transforming Nano Metal Nonselective Particulates into Chemoselective Catalysts for Hydrogenation of Substituted Nitrobenzenes. *ACS Catal.* **2015**, *5* (12), 7114–7121.
(4) Corma, A.; Serna, P. Chemoselective Hydrogenation of Nitro Compounds with Supported Gold Catalysts. *Science* **2006**, *313* (5785), 332–334.
(5) Macino, M.; Barnes, A. J.; Althahban, S. M.; Qu, R.; Gibson, E. K.; Morgan, D. J.; Freakley, S. J.; Dimitratos, N.; Kiely, C. J.; Gao, X.; Beale, A. M.; Bethell, D.; He, Q.; Sankar, M.; Hutchings, G. J. Tuning of Catalytic Sites in Pt/TiO_2 Catalysts for the Chemoselective Hydrogenation of 3-Nitrostyrene. *Nat. Catal.* **2019**, *2* (10), 873–881.
(6) Liu, W.; Feng, H.; Yang, Y.; Niu, Y.; Wang, L.; Yin, P.; Hong, S.; Zhang, B.; Zhang, X.; Wei, M. Highly-Efficient RuNi Single-Atom Alloy Catalysts toward Chemoselective Hydrogenation of Nitroarenes. *Nat. Commun.* **2022**, *13* (1), 3188.
(7) Zhang, L.; Zhou, M.; Wang, A.; Zhang, T. Selective Hydrogenation over Supported Metal Catalysts: From Nanoparticles to Single Atoms. *Chem. Rev.* **2020**, *120* (2), 683–733.
(8) Zhang, J.; Wang, L.; Shao, Y.; Wang, Y.; Gates, B. C.; Xiao, F. A Pd@Zeolite Catalyst for Nitroarene Hydrogenation with High Product Selectivity by Sterically Controlled Adsorption in the Zeolite Micropores. *Angew. Chem. Int. Ed.* **2017**, *56* (33), 9747–9751.
(9) Qu, R.; Macino, M.; Iqbal, S.; Gao, X.; He, Q.; Hutchings, G. J.; Sankar, M. Supported Bimetallic AuPd Nanoparticles as a Catalyst for the Selective Hydrogenation of Nitroarenes. *Nanomaterials* **2018**, *8* (9), 690.
(10) Zhang, S.; Xia, Z.; Ma, Y.; Li, J.; Qu, Y. Competitive Adsorption on $PtCo/CoBO_x$ Catalysts Enables the Selective Hydrogen-Reductive-Imination of Nitroarenes with Aldehydes into Imines. *J. Catal.* **2019**, *374*, 72–81.
(11) Gong, W.; Han, M.; Chen, C.; Lin, Y.; Wang, G.; Zhang, H.; Zhao, H. Rational Design of Cobalt-Platinum Alloy Decorated Cobalt Nanoparticles for One-Pot Synthesis of Imines from Nitroarenes and Aldehydes. *ChemCatChem* **2020**, *12* (23), 5948–5958.
(12) Shen, M.; Afshar, A.; Sinai, N.; Guan, H.; Harris, C.; Rubenstein, B.; Sun, S. Enabling Pd Catalytic Selectivity via Engineering Intermetallic Core@Shell Structure. *ACS Nano* **2024**, *18* (1), 178–185.
(13) Yin, D.; Li, C.; Ren, H.; Liu, J.; Liang, C. Gold-Palladium-Alloy-Catalyst Loaded $UiO\text{-}66\text{-}NH_2$ for Reductive Amination with Nitroarenes Exhibiting High Selectivity. *ChemistrySelect* **2018**, *3* (18), 5092–5097.
(14) Yamanaka, N.; Hara, T.; Ichikuni, N.; Shimazu, S. Chemoselective Synthesis of Imine and Secondary Amine from Nitrobenzene and Benzaldehyde by Ni_3Sn_2 Alloy Catalyst Supported on TiO_2. *Mol. Catal.* **2021**, *505*, 111503.
(15) Chen, C.; Fan, R.; Han, M.; Zhu, X.; Zhang, Y.; Zhang, H.; Zhao, H.; Wang, G. Tunable Synthesis of Imines and Secondary-Amines from Tandem Hydrogenation-Coupling of Aromatic Nitro and Aldehyde over $NiCo_5$ Bi-Metallic Catalyst. *Appl. Catal. B: Environ.* **2021**, *280*, 119448.

(16) Xiang, Y.; Meng, Q.; Li, X.; Wang, J. In Situ Hydrogen from Aqueous-Methanol for Nitroarene Reduction and Imine Formation over an Au–Pd/Al_2O_3 Catalyst. *Chem. Commun.* **2010**, *46* (32), 5918–5920.

(17) Sharif, Md. J.; Yamazoe, S.; Tsukuda, T. Selective Hydrogenation of 4-Nitrobenzaldehyde to 4-Aminobenzaldehyde by Colloidal RhCu Bimetallic Nanoparticles. *Top. Catal.* **2014**, *57* (10–13), 1049–1053.

(18) Santos, L. L.; Serna, P.; Corma, A. Chemoselective Synthesis of Substituted Imines, Secondary Amines, and β-Amino Carbonyl Compounds from Nitroaromatics through Cascade Reactions on Gold Catalysts. *Chem. Eur. J.* **2009**, *15* (33), 8196–8203.

(19) Li, M.; Hao, Y.; Cárdenas-Lizana, F.; Keane, M. A. Gold Promoted Imine Production by Selective Gas Phase Reductive Coupling of Nitrobenzene and Benzaldehyde. *Appl. Catal. A: Gen.* **2017**, *531*, 52–59.

(20) Perret, N.; Wang, X.; Onfroy, T.; Calers, C.; Keane, M. A. Selectivity in the Gas-Phase Hydrogenation of 4-Nitrobenzaldehyde over Supported Au Catalysts. *J. Catal.* **2014**, *309*, 333–342.

(21) Zhao, H.; Li, B.; Zhao, H.; Li, J.; Kou, J.; Zhu, H.; Liu, B.; Li, Z.; Sun, X.; Dong, Z. Construction of a Sandwich-like UiO-66-NH_2@Pt@mSiO_2 Catalyst for One-Pot Cascade Reductive Amination of Nitrobenzene with Benzaldehyde. *J. Colloid Interface Sci.* **2022**, *606*, 1524–1533.

(22) Garg, S.; Xie, Z.; Chen, J. G. Tandem Reactors and Reactions for CO_2 Conversion. *Nat. Chem. Eng.* **2024**, *1* (2), 139–148.

(23) Routh, P. K.; Redekop, E.; Prodinger, S.; Van Der Hoeven, J. E. S.; Lim, K. R. G.; Aizenberg, J.; Nachtegaal, M.; Clark, A. H.; Frenkel, A. I. Restructuring Dynamics of Surface Species in Bimetallic Nanoparticles Probed by Modulation Excitation Spectroscopy. *Nat. Commun.* **2024**, *15* (1), 6736.

(24) Luneau, M.; Shirman, T.; Foucher, A. C.; Duanmu, K.; Verbart, D. M. A.; Sautet, P.; Stach, E. A.; Aizenberg, J.; Madix, R. J.; Friend, C. M. Achieving High Selectivity for Alkyne Hydrogenation at High Conversions with Compositionally Optimized PdAu Nanoparticle Catalysts in Raspberry Colloid-Templated SiO_2. *ACS Catal.* **2020**, *10* (1), 441–450.

(25) van der Hoeven, J. E. S.; Ngan, H. T.; Yan, G.; Aizenberg, J.; Madix, R. J.; Sautet, P.; Friend, C. M. Unraveling 1-Hexene Hydrogenation over Dilute Pd-in-Au Alloys. *J. Phys. Chem. C* **2022**, *126* (37), 15710–15723.

(26) van der Hoeven, J. E. S.; Ngan, H. T.; Taylor, A.; Eagan, N. M.; Aizenberg, J.; Sautet, P.; Madix, R. J.; Friend, C. M. Entropic Control of HD Exchange Rates over Dilute Pd-in-Au Alloy Nanoparticle Catalysts. *ACS Catal.* **2021**, *11* (12), 6971–6981.

(27) Kaiser, S. K.; Van Der Hoeven, J. E. S.; Yan, G.; Lim, K. R. G.; Ngan, H. T.; Garg, S.; Karatok, M.; Aizenberg, M.; Aizenberg, J.; Sautet, P.; Friend, C. M.; Madix, R. J. Identifying the Optimal Pd Ensemble Size in Dilute PdAu Alloy Nanomaterials for Benzaldehyde Hydrogenation. *ACS Catal.* **2023**, *13* (18), 12092–12103.

(28) Lee, J. D.; Miller, J. B.; Shneidman, A. V.; Sun, L.; Weaver, J. F.; Aizenberg, J.; Biener, J.; Boscoboinik, J. A.; Foucher, A. C.; Frenkel, A. I.; van der Hoeven, J. E. S.; Kozinsky, B.; Marcella, N.; Montemore, M. M.; Ngan, H. T.; O'Connor, C. R.; Owen, C. J.; Stacchiola, D. J.; Stach, E. A.; Madix, R. J.; Sautet, P.; Friend, C. M. Dilute

Alloys Based on Au, Ag, or Cu for Efficient Catalysis: From Synthesis to Active Sites. *Chem. Rev.* **2022**, *122* (9), 8758–8808.

(29) Nakaya, Y.; Furukawa, S. Catalysis of Alloys: Classification, Principles, and Design for a Variety of Materials and Reactions. *Chem. Rev.* **2023**, *123* (9), 5859–5947.

(30) Luneau, M.; Lim, J. S.; Patel, D. A.; Sykes, E. C. H.; Friend, C. M.; Sautet, P. Guidelines to Achieving High Selectivity for the Hydrogenation of α,β-Unsaturated Aldehydes with Bimetallic and Dilute Alloy Catalysts: A Review. *Chem. Rev.* **2020**, *120* (23), 12834–12872.

(31) Hannagan, R. T.; Giannakakis, G.; Flytzani-Stephanopoulos, M.; Sykes, E. C. H. Single-Atom Alloy Catalysis. *Chem. Rev.* **2020**, *120* (21), 12044–12088.

(32) Shirman, E.; Shirman, T.; Shneidman, A. V.; Grinthal, A.; Phillips, K. R.; Whelan, H.; Bulger, E.; Abramovitch, M.; Patil, J.; Nevarez, R.; Aizenberg, J. Modular Design of Advanced Catalytic Materials Using Hybrid Organic-Inorganic Raspberry Particles. *Adv. Funct. Mater.* **2018**, *28* (27), 1704559.

(33) Lim, K. R. G.; Kaiser, S. K.; Wu, H.; Garg, S.; O'Connor, C. R.; Reece, C.; Aizenberg, M.; Aizenberg, J. Deconvoluting the Individual Effects of Nanoparticle Proximity and Size in Thermocatalysis. *ACS Nano* **2024**, *18* (24), 15958–15969.

(34) Lim, K. R. G.; Kaiser, S. K.; Wu, H.; Garg, S.; Perxés Perich, M.; Van Der Hoeven, J. E. S.; Aizenberg, M.; Aizenberg, J. Nanoparticle Proximity Controls Selectivity in Benzaldehyde Hydrogenation. *Nat. Catal.* **2024**, *7* (2), 172–184.

(35) Lim, K. R. G.; Aizenberg, M.; Aizenberg, J. Colloidal Templating in Catalyst Design for Thermocatalysis. *J. Am. Chem. Soc.* **2024**, *146* (32), 22103–22121.

(36) Lim, K. R. G.; Kaiser, S. K.; Herring, C. J.; Kim, T.-S.; Perich, M. P.; Garg, S.; O'Connor, C. R.; Aizenberg, M.; Van Der Hoeven, J. E. S.; Reece, C.; Montemore, M. M.; Aizenberg, J. Partial PdAu Nanoparticle Embedding into TiO_2 Support Accentuates Catalytic Contributions from the Au/TiO_2 Interface. *Proc. Natl. Acad. Sci. U.S.A.* **2025**, *122* (2), e2422628122.

(37) van der Hoeven, J. E. S.; Krämer, S.; Dussi, S.; Shirman, T.; Park, K. K.; Rycroft, C. H.; Bell, D. C.; Friend, C. M.; Aizenberg, J. On the Origin of Sinter-Resistance and Catalyst Accessibility in Raspberry-Colloid-Templated Catalyst Design. *Adv. Funct. Mater.* **2021**, *31* (49), 2106876.

(38) Luneau, M.; Guan, E.; Chen, W.; Foucher, A. C.; Marcella, N.; Shirman, T.; Verbart, D. M. A.; Aizenberg, J.; Aizenberg, M.; Stach, E. A.; Madix, R. J.; Frenkel, A. I.; Friend, C. M. Enhancing Catalytic Performance of Dilute Metal Alloy Nanomaterials. *Commun. Chem.* **2020**, *3* (1), 46.

(39) van der Hoeven, J. E. S.; Deng, T.-S.; Albrecht, W.; Olthof, L. A.; van Huis, M. A.; de Jongh, P. E.; van Blaaderen, A. Structural Control over Bimetallic Core–Shell Nanorods for Surface-Enhanced Raman Spectroscopy. *ACS Omega* **2021**, *6* (10), 7034–7046.

(40) Piella, J.; Bastús, N. G.; Puntes, V. Size-Controlled Synthesis of Sub-10-Nanometer Citrate-Stabilized Gold Nanoparticles and Related Optical Properties. *Chem. Mater.* **2016**, *28* (4), 1066–1075.

(41) Pretzer, L. A.; Song, H. J.; Fang, Y.-L.; Zhao, Z.; Guo, N.; Wu, T.; Arslan, I.; Miller, J. T.; Wong, M. S. Hydrodechlorination Catalysis of Pd-on-Au Nanoparticles Varies with Particle Size. *J. Catal.* **2013**, *298*, 206–217.

(42) Ishida, T.; Murayama, T.; Taketoshi, A.; Haruta, M. Importance of Size and Contact Structure of Gold Nanoparticles for the Genesis of Unique Catalytic Processes. *Chem. Rev.* **2020**, *120* (2), 464–525.

(43) Foucher, A. C.; Ngan, H. T.; Shirman, T.; Filie, A.; Duanmu, K.; Aizenberg, M.; Madix, R. J.; Friend, C. M.; Aizenberg, J.; Sautet, P.; Stach, E. A. Influence of Pd Concentration in Au–Pd Nanoparticles for the Hydrogenation of Alkynes. *ACS Appl. Nano Mater.* **2023**, *6* (24), 22927–22938.

(44) Lim, K. R. G.; Shirman, T.; Toops, T. J.; Alvarenga, J.; Aizenberg, M.; Aizenberg, J. Active and Stable PtPd Diesel Oxidation Catalysts under Industry-defined Test Protocols. *ChemSusChem* **2025**, *18*, e202500295.

(45) Yu, W.-Y.; Mullen, G. M.; Mullins, C. B. Interactions of Hydrogen and Carbon Monoxide on Pd–Au Bimetallic Surfaces. *J. Phys. Chem. C* **2014**, *118* (4), 2129–2137.

(46) Zhu, B.; Thrimurthulu, G.; Delannoy, L.; Louis, C.; Mottet, C.; Creuze, J.; Legrand, B.; Guesmi, H. Evidence of Pd Segregation and Stabilization at Edges of AuPd Nano-Clusters in the Presence of CO: A Combined DFT and DRIFTS Study. *J. Catal.* **2013**, *308*, 272–281.

(47) Wei, T.; Wang, J.; Goodman, D. W. Characterization and Chemical Properties of Pd−Au Alloy Surfaces. *J. Phys. Chem. C* **2007**, *111* (25), 8781–8788.

(48) Zeinalipour-Yazdi, C. D.; Willock, D. J.; Thomas, L.; Wilson, K.; Lee, A. F. CO Adsorption over Pd Nanoparticles: A General Framework for IR Simulations on Nanoparticles. *Surf. Sci.* **2016**, *646*, 210–220.

(49) Luneau, M.; Shirman, T.; Filie, A.; Timoshenko, J.; Chen, W.; Trimpalis, A.; Flytzani-Stephanopoulos, M.; Kaxiras, E.; Frenkel, A. I.; Aizenberg, J.; Friend, C. M.; Madix, R. J. Dilute Pd/Au Alloy Nanoparticles Embedded in Colloid-Templated Porous SiO_2: Stable Au-Based Oxidation Catalysts. *Chem. Mater.* **2019**, *31* (15), 5759–5768.

(50) Childers, D. J.; Schweitzer, N. M.; Shahri, S. M. K.; Rioux, R. M.; Miller, J. T.; Meyer, R. J. Evidence for Geometric Effects in Neopentane Conversion on PdAu Catalysts. *Catal. Sci. Technol.* **2014**, *4* (12), 4366–4377.

(51) Zhou, C.; Ngan, H. T.; Lim, J. S.; Darbari, Z.; Lewandowski, A.; Stacchiola, D. J.; Kozinsky, B.; Sautet, P.; Boscoboinik, J. A. Dynamical Study of Adsorbate-Induced Restructuring Kinetics in Bimetallic Catalysts Using the PdAu(111) Model System. *J. Am. Chem. Soc.* **2022**, *144* (33), 15132–15142.

(52) Wang, H.; Wang, C.; Yan, H.; Yi, H.; Lu, J. Precisely-Controlled Synthesis of Au@Pd Core–Shell Bimetallic Catalyst via Atomic Layer Deposition for Selective Oxidation of Benzyl Alcohol. *J. Catal.* **2015**, *324*, 59–68.

(53) Menegazzo, F.; Canton, P.; Pinna, F.; Pernicone, N. Bimetallic Pd–Au Catalysts for Benzaldehyde Hydrogenation: Effects of Preparation and of Sulfur Poisoning. *Catal. Commun.* **2008**, *9* (14), 2353–2356.

(54) Torres, C.; Campos, C.; Fierro, J. L. G.; Oportus, M.; Reyes, P. Nitrobenzene Hydrogenation on Au/TiO_2 and Au/SiO_2 Catalyst: Synthesis, Characterization and Catalytic Activity. *Catal. Lett.* **2013**, *143* (8), 763–771.

(55) Boronat, M.; Concepción, P.; Corma, A.; González, S.; Illas, F.; Serna, P. A Molecular Mechanism for the Chemoselective Hydrogenation of Substituted Nitroaromatics with Nanoparticles of Gold on TiO_2 Catalysts: A Cooperative Effect between Gold and the Support. *J. Am. Chem. Soc.* **2007**, *129* (51), 16230–16237.

(56) Li, M.; Wang, X.; Cárdenas-Lizana, F.; Keane, M. A. Effect of Support Redox Character on Catalytic Performance in the Gas Phase Hydrogenation of Benzaldehyde and Nitrobenzene over Supported Gold. *Catal. Today* **2017**, *279*, 19–28.

(57) Shimizu, K.; Miyamoto, Y.; Kawasaki, T.; Tanji, T.; Tai, Y.; Satsuma, A. Chemoselective Hydrogenation of Nitroaromatics by Supported Gold Catalysts: Mechanistic Reasons of Size- and Support-Dependent Activity and Selectivity. *J. Phys. Chem. C* **2009**, *113* (41), 17803–17810.

(58) Hao, Y.; Pischetola, C.; Cárdenas-Lizana, F.; Keane, M. A. Selective Liquid Phase Hydrogenation of Benzaldehyde to Benzyl Alcohol Over Alumina Supported Gold. *Catal. Lett.* **2020**, *150* (3), 881–887.

(59) Bijl, M.; Lim, K. R. G.; Garg, S.; Nicolas, N. J.; Visser, N. L.; Aizenberg, M.; Van Der Hoeven, J. E. S.; Aizenberg, J. Controlling Nanoparticle Placement in Au/TiO_2 Inverse Opal Photocatalysts. *Nanoscale* **2024**, *16* (29), 13867–13873.

(60) Michel, V.; Dorothée, L.; Christophe, G. Use of Competitive Kinetics for the Understanding of Deep Hydrodesulfurization and Sulfide Catalysts Behavior. *Appl. Catal. B: Environ.* **2012**, *128*, 3–9.

(61) Pyatnitsky, Yu. I. Some New Approaches to the Competitive Catalytic Reaction Kinetics. *Appl. Catal. A: Gen.* **1994**, *113* (1), 9–28.

(62) Lee, A. F.; Hackett, S. F. J.; Hutchings, G. J.; Lizzit, S.; Naughton, J.; Wilson, K. In Situ X-Ray Studies of Crotyl Alcohol Selective Oxidation over Au/Pd(111) Surface Alloys. *Catal. Today* **2009**, *145* (3–4), 251–257.

(63) Routh, P. K.; Liu, X.; Redekop, E.; Lim, J. S.; Prodinger, S.; Van Der Hoeven, J. E. S.; Aizenberg, J.; Nachtegaal, M.; Clark, A. H.; Sautet, P.; Frenkel, A. I. Unraveling the Kinetics of Hydride Formation and Decomposition at Pd–Au Bimetallic Interfaces: A Combined Spectroscopic and Computational Study. *J. Am. Chem. Soc.* **2025**, *147* (13), 11378–11389.

(64) Ouyang, M.; Papanikolaou, K. G.; Boubnov, A.; Hoffman, A. S.; Giannakakis, G.; Bare, S. R.; Stamatakis, M.; Flytzani-Stephanopoulos, M.; Sykes, E. C. H. Directing Reaction Pathways via in Situ Control of Active Site Geometries in PdAu Single-Atom Alloy Catalysts. *Nat. Commun.* **2021**, *12* (1), 1549.

(65) Lim, K. R. G.; Owen, C. J.; Kaiser, S. K.; Routh, P. K.; Mendoza, M.; Park, K. K.; Kim, T.-S.; Garg, S.; Gardener, J. A.; Russotto, L.; O'Connor, C. R.; Bijl, M.; Aizenberg, M.; Reece, C.; Lee, J. D.; Frenkel, A. I.; Kozinsky, B.; Aizenberg, J. Nanoscale Wetting Phenomena Controls Reactive Pd Ensembles in Synthesis of Dilute PdAu Alloy Catalysts. In revision.

(66) Owen, C. J.; Russotto, L.; O'Connor, C. R.; Marcella, N.; Johansson, A.; Musaelian, A.; Kozinsky, B. Atomistic Evolution of Active Sites in Multi-Component Heterogeneous Catalysts. arXiv July 18, 2024.

(67) Marcella, N.; Lim, J. S.; Płonka, A. M.; Yan, G.; Owen, C. J.; van der Hoeven, J. E. S.; Foucher, A. C.; Ngan, H. T.; Torrisi, S. B.; Marinkovic, N. S.; Stach, E. A.; Weaver, J.

F.; Aizenberg, J.; Sautet, P.; Kozinsky, B.; Frenkel, A. I. Decoding Reactive Structures in Dilute Alloy Catalysts. *Nat. Commun.* **2022**, *13* (1), 832.

(68) El Berch, J. N.; Salem, M.; Mpourmpakis, G. Advances in Simulating Dilute Alloy Nanoparticles for Catalysis. *Nanoscale* **2025**, *17* (4), 1936–1953.

(69) Maroun, F.; Ozanam, F.; Magnussen, O. M.; Behm, R. J. The Role of Atomic Ensembles in the Reactivity of Bimetallic Electrocatalysts. *Science* **2001**, *293* (5536), 1811–1814.

(70) Wang, Y.; Cao, L.; Libretto, N. J.; Li, X.; Li, C.; Wan, Y.; He, C.; Lee, J.; Gregg, J.; Zong, H.; Su, D.; Miller, J. T.; Mueller, T.; Wang, C. Ensemble Effect in Bimetallic Electrocatalysts for CO_2 Reduction. *J. Am. Chem. Soc.* **2019**, *141* (42), 16635–16642.

(71) Ricciardulli, T.; Gorthy, S.; Adams, J. S.; Thompson, C.; Karim, A. M.; Neurock, M.; Flaherty, D. W. Effect of Pd Coordination and Isolation on the Catalytic Reduction of O_2 to H_2O_2 over PdAu Bimetallic Nanoparticles. *J. Am. Chem. Soc.* **2021**, *143* (14), 5445–5464.

(72) Akinsanya, O. O.; Patel, D. M.; O'Connor, C. R.; Perich, M. P.; Van Der Hoeven, J. E. S.; Reece, C.; Roling, L. T.; Eagan, N. M. Understanding the Promotional Role of Pd in Oxidative Alcohol Coupling Reactions over Dilute PdAu Alloys. *J. Catal.* **2025**, *443*, 115942.

(73) Sharma, A. K.; Mehara, P.; Das, P. Recent Advances in Supported Bimetallic Pd–Au Catalysts: Development and Applications in Organic Synthesis with Focused Catalytic Action Study. *ACS Catal.* **2022**, *12* (11), 6672–6701.

(74) Liu, L.; Corma, A. Bimetallic Sites for Catalysis: From Binuclear Metal Sites to Bimetallic Nanoclusters and Nanoparticles. *Chem. Rev.* **2023**, *123* (8), 4855–4933.

(75) Crawley, J. W. M.; Gow, I. E.; Lawes, N.; Kowalec, I.; Kabalan, L.; Catlow, C. R. A.; Logsdail, A. J.; Taylor, S. H.; Dummer, N. F.; Hutchings, G. J. Heterogeneous Trimetallic Nanoparticles as Catalysts. *Chem. Rev.* **2022**, *122* (6), 6795–6849.

(76) Wrasman, C. J.; Riscoe, A. R.; Lee, H.; Cargnello, M. Dilute Pd/Au Alloys Replace Au/TiO_2 Interface for Selective Oxidation Reactions. *ACS Catal.* **2020**, *10* (3), 1716–1720.

(77) Wrasman, C. J.; Boubnov, A.; Riscoe, A. R.; Hoffman, A. S.; Bare, S. R.; Cargnello, M. Synthesis of Colloidal Pd/Au Dilute Alloy Nanocrystals and Their Potential for Selective Catalytic Oxidations. *J. Am. Chem. Soc.* **2018**, *140* (40), 12930–12939.

(78) Minne, A. P.; Maxson, T.; Szilvási, T.; Harris, J. W. Selective Vapor-Phase Formation of Dimethylformamide *via* Oxidative Coupling of Methanol and Dimethylamine over Bimetallic Catalysts. *Catal. Sci. Technol.* **2024**, *14* (6), 1534–1549.

(79) Shirman, T.; Toops, T. J.; Shirman, E.; Shneidman, A. V.; Liu, S.; Gurkin, K.; Alvarenga, J.; Lewandowski, M. P.; Aizenberg, M.; Aizenberg, J. Raspberry Colloid-Templated Approach for the Synthesis of Palladium-Based Oxidation Catalysts with Enhanced Hydrothermal Stability and Low-Temperature Activity. *Catal. Today* **2021**, *360*, 241–251.

(80) Meincke, T.; Jordan, M.; Vogel, N.; Klupp Taylor, R. N. On the Size-Determining Role of the Comonomer in the Nucleation and Growth of Cationic Polystyrene Latex via Emulsion Polymerization. *Macromol. Chem. Phys.* **2018**, *219* (4), 1700457.

DATA AVAILABILITY

Raw data used to prepare the figures in the main text will be made available in a public repository after article acceptance.